Finite Elements in Analysis and Design 221 (2023) 103960

Contents lists available at ScienceDirect

Finite Elements in Analysis & Design

journal homepage: www.elsevier.com/locate/finel

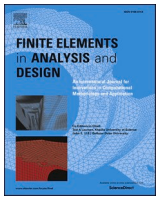

High-accurate FE simulation on compressive behavior of steel cruciform column with welding imperfection

Yuxuan Cheng, Shuhei Nozawa, Mikihito Hirohata *

Department of Civil Engineering, Osaka University, Suita 5650871, Japan

ARTICLE INFO

Keywords:
Finite element analysis
Steel structures
Load-bearing capacity
Welding
Initial imperfection

ABSTRACT

Due to its various advantages, welding is commonly used in the construction for steel connection. However, the local temperature difference in the welding causes welding deformation and residual stress. The welding deformation and residual stress can significantly impact the load-bearing performance of members. Therefore, it is important to evaluate those behaviors with high precision. In the previous studies, thermal elastic-plastic analysis was used to evaluate welding deformation and residual stress in simulated welded specimens and the compressive simulation was applied to obtain, for example, the load-bearing performance. Nevertheless, there are limitations in assessing structures made up of thin plates. This is because the simulation of welding is typically modeled using solid elements, while the simulation of loading analysis uses shell elements. As a result, these analysis steps are not directly related, leading to deficiencies in the evaluation process. In this study, the solid element model and shell element model were modeled to simulate the welding deformation and residual stress. The corresponding load-bearing capacity results obtained from the continuous loading analysis were compared with the results from experiment to verify the consistency. According to the results, shell models that perform welding analysis simulation followed by continuous compressive analysis are better able to replicate experimental results in terms of out-of-plane deformation and maximum load-carrying capacity under compressive analysis. This is in contrast to solid models, which fall short in reproducing the same results. Moreover, the shell model is also more efficient than the solid model in terms of time saved during analysis and calculation.

1. Introduction

Welding is widely used for joining members in the construction of steel structures such as bridges and ships. The popularity of welding can be attributed to its versatility in narrow spaces, high joint efficiency, and design flexibility. However, welding can cause deformation and residual stress owing to the temperature difference within the component resulting from localized heat input. Welding deformation affects the stiffness of members as an initial deflection [1]. Regarding welding residual stress, the localized heat input causes the welded part to expand during the welding process, which is then constrained by the surrounding base metal during cooling. As a result, high tensile stress is generated near the welded part, while compressive stress is produced away from it to counterbalance the tensile stress. Additionally, the presence of compressive residual stress can significantly impact the load-bearing performance of members [2].

When considering the initial deflection and residual stress, sine waves are often used to model the initial deflection in finite element analysis, despite its typical use for evaluating the load-bearing performance of steel structures [3]. A rectangular distribution is frequently employed as a simplified model when incorporating welding residual stress [4]. Although the initial deflection (welding deformation) and residual stress essentially have a corresponding relationship, in most cases, they are considered independent and introduced separately for analysis. Such methods may not correctly consider the effects of initial imperfections on the mechanical behavior of members. Specifically, accurately reproducing welding deformation and residual stress is crucial, as it requires introducing them as initial imperfections with consistency and then analyzing the load-bearing performance. Thermal elastic–plastic analysis is a high-accuracy technique for predicting welding deformation and residual stress [5]. Welding simulations using thermal elastic–plastic analysis generally use three-dimensional solid elements to reproduce the shape of the weld metal and groove [6]. However, when simulating the mechanical behavior of a steel structure

* Corresponding author.
E-mail address: hirohata@civil.eng.osaka-u.ac.jp (M. Hirohata).

https://doi.org/10.1016/j.finel.2023.103960
Received 19 December 2022; Received in revised form 20 March 2023; Accepted 28 April 2023
Available online 3 May 2023

composed of relatively thin plates using elastic–plastic finite displacement analysis, planar shell elements are commonly used to suitably reproduce bending deformation [7]. Specifically, by comparing solid elements that are generally applied in thermal elastic–plastic analysis to predict welding deformation and residual stress, shell elements are primarily used in elastic–plastic finite displacement analysis to evaluate the load-bearing performance of steel structures. Owing to variations in the types of elements used, the analyses were carried out separately, without any connection to the preceding analysis step.

To address these issues, Hirohata et al. proposed a new welding process analysis method that uses shell elements [8–10]. The study revealed that utilizing shell elements to model welding for butt joints and T-joints can accurately predict welding deformation and residual stress, comparable to the results obtained when using solid elements. In addition, utilizing shell elements with a limited number of nodes resulted in a notable enhancement in computation speed, in contrast to the use of solid elements.

This study utilized a simulation method that employs shell elements, which had been proposed in previous research, to replicate deformation and residual stress during welding processes. Moreover, the study explored a method for continuous loading analysis. To examine a cruciform cross-sectional column subjected to monotonic compressive loads, the analysis of the welding process during fabrication of the specimen was used to obtain the initial imperfections of deformation and residual stress. These imperfections were then introduced, and the loading process was analyzed continuously. By comparing the results with experimental data, the accuracy of introducing welding deformation and residual stress as initial imperfections without contradictions was confirmed, and the precision of the analysis was evaluated.

2. Experimental procedure

2.1. Specimen

The steel cruciform columns shown in Fig. 1 were prepared as the specimens for this study. The shapes and dimensions of the specimens were assumed as steel I-section girder ends subjected to a concentrated compressive load designed according to the Specifications for Highway Bridges [11]. The plate material was SM400B. The thicknesses of the flanges, web, and stiffeners were 19, 6, and 9 mm, respectively. The plates were joined via gas metal arc welding using a welding wire specified by JIS YGW12. The welding wire was 1.2 mm. The welding process utilized a voltage of 19.5 V and a current of 250 A. The average welding speed during the welding of the vertical plates (web and stiffener) was 7.5 mm/s. Previous research [12–14] has demonstrated that the welding sequence and direction significantly influence the magnitude and distribution of the welding deformation. Based on these conclusions, a welding sequence was adopted, as shown in Fig. 2(a). A welding sequence in the co-direction was used between the flanges and vertical plates, as shown in the 1st–16th welding passes, and welding along the opposite direction was used between the web and stiffener, as shown in the 17th–20th welding passes. This study did not prioritize analyzing the extent of deformation resulting from the welding sequence, as the simulation model considered the initial deformation introduced during welding. Table 1 lists the mechanical properties (mill sheet and catalog values) of the materials used for each specimen. Two specimens were used in this study.

Fig. 1. Experimental specimen overview.

2.2. Measurement

As shown in Fig. 2 (b), six thermocouples were attached to the surface of the web and stiffener at the center of the specimen along the height direction (y = 300 (mm)). The temperature histories during welding were measured using these thermocouples.

Out-of-plane deformations in the web and stiffeners caused by welding were measured using a dial gauge. The measurement locations were at the free edges of each panel, as shown in Fig. 2 (b) (y = 5, 200, 300, 400, 500, and 595 mm). The free edges of the web are referred to as W-1 and W-2. The free edges of the stiffeners are referred to as S-1 and S-2.

The welding residual stresses were measured using an X-ray diffractometer (μ-X360s by Pulstec Industrial Co., Ltd.). Owing to the restrictions of the measuring device, it was difficult to measure the joint side between the web and stiffeners. Therefore, the residual stresses were measured at the center of the free edges in the vertical direction (y = 300 (mm)) as shown in Fig. 2 (a). The stress components in the column height direction (y-direction) were measured. This direction corresponded to the loading direction in the compressive experiment that is described later. The stress component in the loading direction significantly affected the load-bearing performance of the cruciform column.

2.3. Compressive loading experiment

Compressive loading experiments were conducted on these two specimens. A static loading machine was used to apply a monotonic compressive load along the axial direction of the specimen. Fig. 3 shows the results of the loading experiment. Displacement in the loading direction was measured at two diagonal positions between the edges of the upper and lower flanges. The out-of-plane displacements of the web and stiffeners were measured at the free edges of each panel at mid-height of the specimen (y = 300 (mm)).

3. Welding and loading analysis procedure

3.1. Model analysis through solid elements

The commercial software ABAQUS 6.14 was used for the thermal elastic–plastic analysis. The coupled temperature and displacement functions were selected to simulate the welding process. Fig. 4 shows the FE simulation model assembled using solid elements with eight nodes to reproduce the welding and loading procedures of the experimental specimen (i.e., the solid model). The mesh dimensions for the area along the weld line connecting the flanges to the web plates, and for the flanges to the stiffener plates, are approximately 8.7 mm and 10.1 mm, respectively. The mesh size in the direction perpendicular to the weld line between the vertical plates themselves is approximately 7.8 mm. The number of mesh divisions in the plate thickness direction was four for all flanges, webs, and stiffeners, which implies that the mesh size in the web thickness direction was 1.5 mm, and the mesh size in the

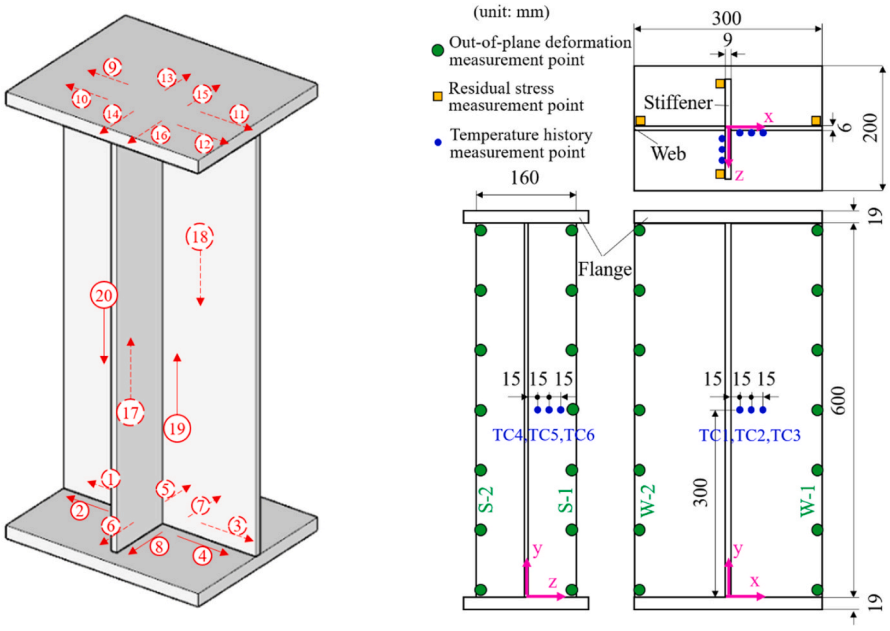

(a) Welding sequence (b) Measurement location on specimen

Fig. 2. Welding sequence and measurement location.

Table 1
Steel material information.

	Chemical composition (mass %)					Mechanical properties		
	C (x100)	Si (x100)	Mn (x100)	P (x1000)	S (x1000)	Yield Strength (N/mm^2)	Tensile Strength (N/mm^2)	Elongation (%)
Flange	13	20	100	18	5	315	442	34
Web	10	21	95	14	4	353	446	33
Stiffener	14	20	82	18	4	280	446	32
Weld metal[a]	2–15	50–100	125–200	<30	<30	390	490 (490–670)	18

[a] Catalog values are given in parentheses.

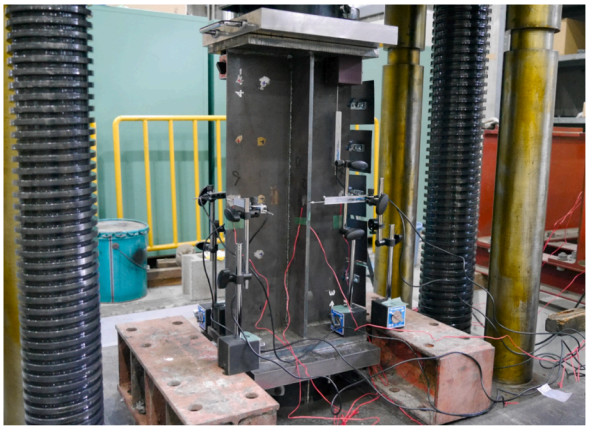

Fig. 3. Compressive experimental setup.

stiffener thickness direction was 2.25 mm. The analysis results showed almost no difference in the analysis results even when a model with a finer mesh division was used. Thus, the mesh division shown in Fig. 4 was appropriate.

The analytical conditions are listed in Table 2. The von Mises yield criterion and the isotropic hardening rule were used. The rigid body movement of the specimen was avoided by using eight metal constraints during welding. The web was restrained using four metal constraints to maintain the web vertically during the fillet welding process. The eight metal constraints were removed after the tack welds were completed. This indicates the existence of an uncontacted gap between the flange surface and vertical plate edges, except for the metal constraints placed before the welding process. Thus, in our simulation model, a gap of 0.1 mm was provided at the boundary of each joined steel plate at the welding parts in the analysis model, as shown in Fig. 4(b).

To prevent the vertical plate from being embedded in the base plate (flanges) during the compression simulation, the simulation model utilized 'Hard' contact conditions between the surfaces, which governed their normal interaction behavior. Additionally, the model considered friction with a coefficient of 0.5 to govern the tangential interaction behavior. In addition, rigid-body displacement was fixed as the mechanical boundary condition. In the solid model, heat transfer to the air from the outer surface of the model was considered as the thermal interaction behavior.

The section shape of the heat input element corresponding to the weld bead was a right-angled isosceles triangle with an edge of 7 mm between the flange and the web or stiffener. The distance between the web and the stiffener was 4.5 mm. The solid model's weld bead design resembled that of the experimental specimen.

Based on previous studies, the stress–strain relationships of each material are shown in Fig. 5 [15]. Other material properties and physical

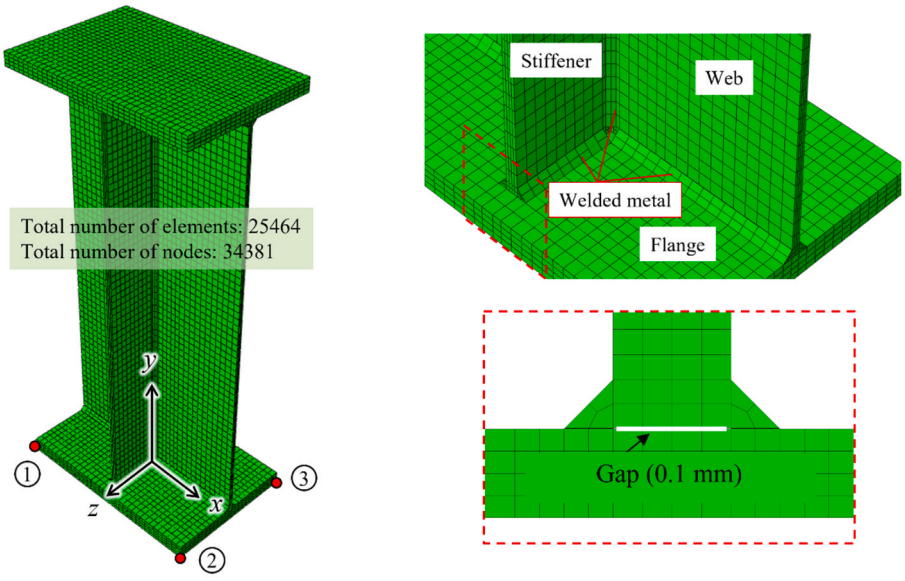

(a) Analysis model overview (b) Welded part of model

Fig. 4. Meshed model using solid element.

Table 2
Analysis conditions of model using solid element.

Analysis conditions setting	Specific description
Element type	8 node reduction integral solid element
Mechanical boundary conditions	*x*-direction displacement: Fix at ①
	y-direction displacement: Fix at ①, ②, ③
	z-direction displacement: Fix at ①, ②
Thermal boundary conditions	Surface heat transfer
Weld line direction mesh size	Flange-web: 8.7 mm
	Flange-stiffener: 7.8 mm
	Web-stiffener:10.1 mm
Physical characteristic value	Temperature-dependent type
Hardening rule	Isotropic hardening rule
Heat input method	Body heat flux
Heat source generation and transfer	Element birth function, moving heat sources
Supplementary conditions	Consider geometric non-linearity

constants are shown in Fig. 6 by referring to previous studies [16]. Previous studies involving welding simulation problems provided evidence for the validity of these material properties and physical constants [8–10,17–19].

The total heat input during welding was calculated using Eq. (1). The voltage, current, and speed were determined based on experimental conditions. The body heat flux was applied to the weld bead elements by considering the step-by-step movement and generation of the heat source using the element birth function. In addition, considering each specific meshed element, the thermal load of each element was set, as shown in Eq. (2). Among them, $\boldsymbol{S}$ is the cross-sectional area of each heat input element and $\boldsymbol{l}$ is the length of each heat input element.

$$\boldsymbol{Q} = \frac{\boldsymbol{\eta EI}}{\boldsymbol{v}} \tag{1}$$

$\boldsymbol{Q}$: Heat input (J/mm)
$\boldsymbol{\eta}$: Thermal efficiency
$\boldsymbol{E}$: Welding voltage (V)
$\boldsymbol{I}$: Welding current (A)
$\boldsymbol{v}$: Welding speed (mm/s)

$$\boldsymbol{q}_{solid} = \boldsymbol{\eta} \times \frac{\boldsymbol{EI}}{\boldsymbol{Sl}} \tag{2}$$

3.2. Model analysis through shell elements

Fig. 7 shows the analysis model assembled using the four nodes of shell elements (i.e., the shell model). A simulation method was proposed using shell elements to weld T-section joints [10]. In the shell model, the degrees of freedom of the thermal load input at each integration point were controlled so that the shape of the heating area converged with that of the actual heating area of the experimental specimen. As shown in Fig. 8, the weld bead shape was considered by changing the thicknesses of the elements corresponding to the weld bead parts. The shapes of the two steps above and below were simulated such that the overall simulated shape resembled an equilateral right triangle. In addition, to ensure that the position of the integration point corresponded to the part of the weld metal, the number of integration points in the thickness direction of each plate was adjusted. The numbers of the integration points in the above and below steps of the weld bead parts were 7 and 9 while the number of the integration points in the base metal parts was 5. For the webs and stiffeners, the center of the plate thickness was used as the reference surface, and for the flanges, the welded side surface was used as the reference surface.

The degrees of freedom of the thermal load input at each integration point were controlled such that the shape of the heating area converged with that of the actual heating area of the experimental specimen. The concentrated and surface heat fluxes were calculated and applied to the integration points corresponding to the weld bead, as shown in Eq. (3). The heat energy applied to the integration points could be directly transferred to the base metal of the vertical plate; thus, the heat input value for each integration point was calculated using Eq. (4). In this case, the authors assumed a heat distribution coefficient of 1, as all heat fluxes could be represented and transferred by a concentrated heat flux. The total heat input was denoted by $\boldsymbol{Q}$, while $\boldsymbol{\eta}$ represented thermal efficiency, and n referred to the number of integration points in the heat input part.

However, heat energy was not transferred to the horizontal web plate, as shown in Fig. 8(a) and (b). To replicate the heat transfer from the weld bead to the base metal of the horizontal web plate, the contact parts between the weld bead and the horizontal web and stiffener plates were subject to both concentrated and surface heat fluxes. In contrast,

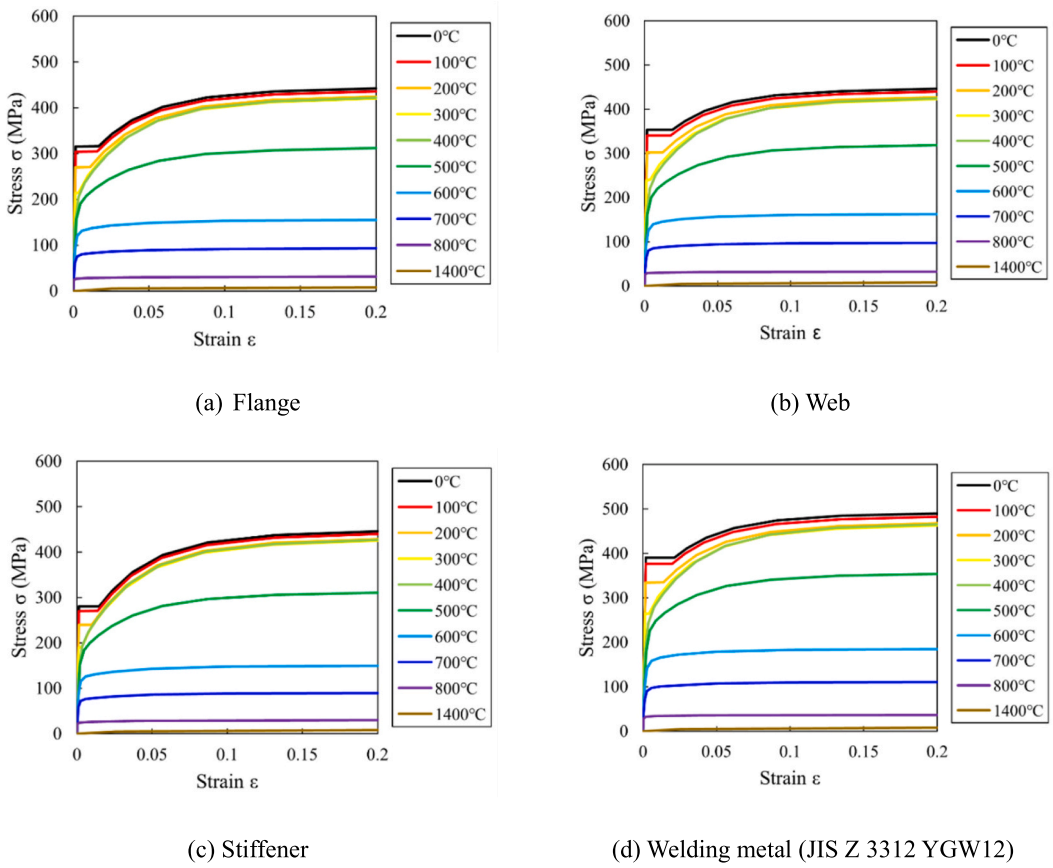

(a) Flange (b) Web

(c) Stiffener (d) Welding metal (JIS Z 3312 YGW12)

Fig. 5. Stress–strain curve of steel materials.

the weld bead parts between the base metal and the vertical plates were only subjected to concentrated heat flux. Because the area of the contact surface between the weld bead and vertical plate was the same as that between the weld bead and horizontal plate, the heat energy calculated using Eq. (3) was uniformly divided into concentrated heat flux and surface heat flux. The magnitude of the concentrated heat flux was calculated by dividing the distributed heat energy by the number of integration points, as shown in Eq. (4). The magnitude of the surface heat flux was calculated by dividing the distributed heat energy by the contact surface area in Eq. (4), where $\boldsymbol{S}$ is the heat input surface area. Thus, in this case, heat distribution coefficient $\boldsymbol{\alpha}$ is assumed to be 0.5 in Eqs. (4) and (5). Based on the above reasons, applying the surface heat flux to the stiffener plate will make the simulation results more accurate and compensate for the adverse effects of the shell model having only one element in its thickness.

The simulation model accounted for the movement of the heat source, but it did not consider the generation of the heat input element.

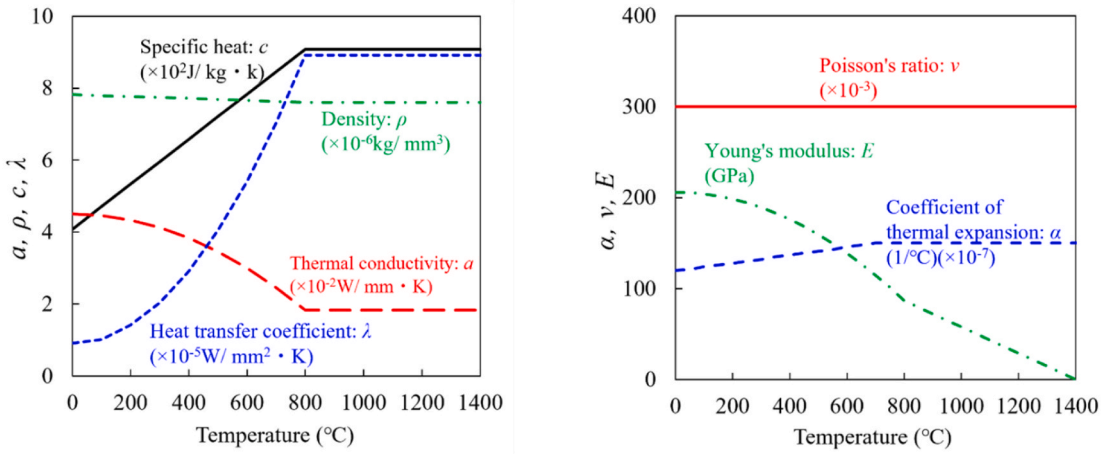

(a) Temperature dependence of physical constants (b) Temperature dependence of mechanical properties

Fig. 6. Material properties and the physical constants.

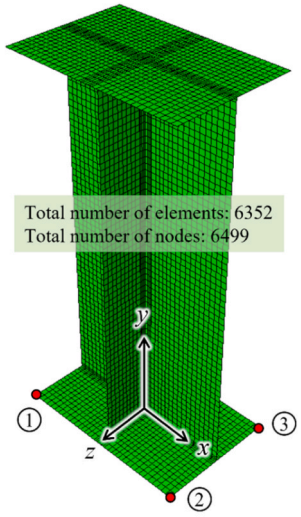

Fig. 7. Shell model overview.

$$q_{shell} = q_{concentrated} + q_{surface} \tag{3}$$

$$q_{concentrated} = \alpha \times \frac{\eta Q}{n} \tag{4}$$

$$q_{surface} = (1-\alpha)\frac{\eta Q}{S} \tag{5}$$

The physical constants and mechanical properties used were identical to those of the solid model. In addition to the solid model, the von Mises yield criterion and the isotropic hardening rule were used in the shell model. Geometric nonlinearity was also considered. The boundary conditions were identical to those used for the solid models. For the mechanical boundary conditions, the rigid body displacement of the model was fixed. Heat transfer to the air from the outer surface of the model was considered as a thermal boundary condition.

3.3. Adjustment of initial deflection

In this study, the effects of welding deformation and residual stress on the compressive behavior of steel structural members were investigated. Furthermore, a method for reproducing this effect was examined through a numerical simulation. In addition, the feasibility of the proposed shell model was investigated.

Although welding deformation and residual stress have complex distributions, previous studies have considered this status by idealizing and simplifying numerical simulations. However, the idealized and simplified deformation and residual stress may deviate from the initial imperfections in actual structural members. It is difficult to determine whether this introduction method has been sufficiently rationalized [20]. Therefore, based on numerical simulations that consider appropriate methods for more precise initial imperfections, it is necessary to improve the accuracy of the load-bearing capacity analysis of steel structural members.

To reproduce the experimentally obtained welding out-of-plane deformation precisely, the initial out-of-plane deformation of the analysis model was adjusted as follows:

As Fig. 9 shown below, first, the deformation values $\boldsymbol{w_e}$ of the nodes corresponding to free edges in the model were obtained using the Akima interpolation method [21].

Second, the difference $\boldsymbol{d}$ between the deformation after the welding simulation $\boldsymbol{w_a}$ and the deformation before the welding simulation $\boldsymbol{w_0}$ was calculated and regarded as the difference caused by the welding heat input in the non-initial deflection model, as shown in Eq. (6). Subsequently, the deformation results $\boldsymbol{d}$ caused by the heat input during the welding process were subtracted from the deformation results after the welding experiments $\boldsymbol{w_e}$. The initial deformation $\boldsymbol{w_0'}$ at the position of each node on the free edge was obtained, as shown in Eq. (7).

Finally, for every node with the same height, the amount of deformation of the free edge was maximized, and an initial deformation proportional to the distance from the center was introduced.

Subsequently, the initial deformation values of each node, which were calculated previously, were incorporated into the new assembly model without welding. Subsequently, welding and compressive simulations were performed sequentially. In this manner, the model and analysis results with initial deflection were obtained. The analysis was performed by considering the adjusted initial deflection such that the out-of-plane welding deformation obtained by the analysis was more accurate.

$$d = w_a\,(x_a, y_a, z_a) - w_0\,(x_0, y_0, z_0) \tag{6}$$

$$w_0{}'\,(x_0', y_0', z_0') = w_e\,(x_e, y_e, z_e) - d \tag{7}$$

3.4. Compressive loading analysis

A compressive load was applied after simulating the welding process of the specimen using thermal elastic-plastic analysis. Table 3 and

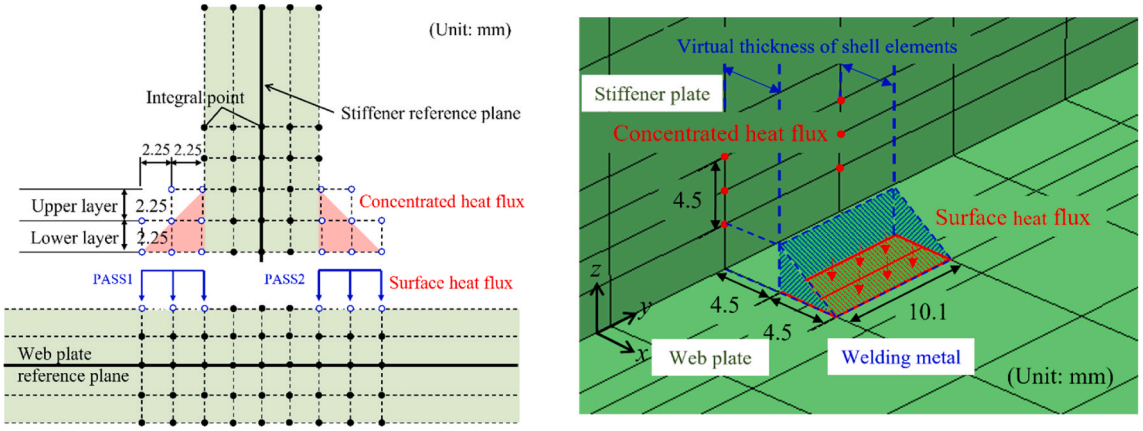

(a) Shell model heat input region

(b) Shell model heat input region overview

Fig. 8. Shell model overview.

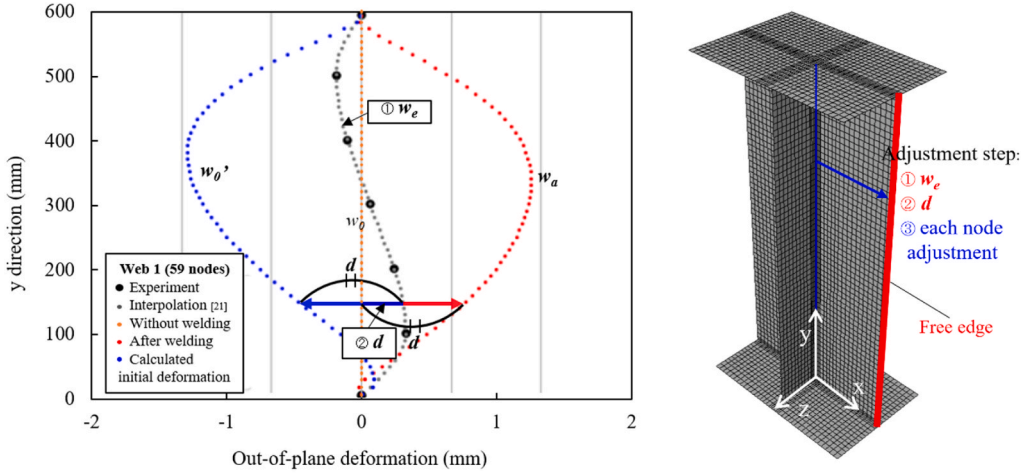

Fig. 9. Adjustment method for initial deformation.

Fig. 10 show the mechanical boundary conditions for the compressive loading analysis. The displacement in the *y*-direction was fixed at the bottom of the lower flange of each model. The load was applied via forced displacement along the *y*-direction to the top surface of the upper flange. During the loading process, to suppress the torsion of the upper and lower flanges, the horizontal displacement was constrained at two points on each of the upper and lower flanges in the *x* and *z* directions. The stress–strain relationship used was interpolated from the relationship shown in Fig. 5 and pertained to room temperature conditions.

4. Results and discussion

4.1. Welding temperature history

As a representative example, two of the four welding temperature histories obtained from the experiment and analysis between the web and stiffener were selected, as shown in Figs. 11 and 12. As the difference in the experimental results between the two specimens was small, the results for one specimen were simulated using the analysis. These figures show the first and second welding passes of the four welding processes on the stiffener plates. By setting the thermal efficiency to 0.75 for the solid model and 0.8 for the shell model, the experimental results were accurately reproduced.

Please note that during the welding process, not all the energy calculated from the current, voltage, and welding speed is transferred to the steel plate due to energy losses caused by spatter and heat radiation. To account for these losses and to adjust for the differences in heat-input volumes and the number of integration points between the solid and shell models, thermal efficiency coefficients were adjusted to two different values in Eq. (1) to ensure that both models accurately replicated the temperature distribution of the experimental specimens. Typically, the thermal efficiency of arc welding falls between 65% and 80% [22]. Thus, by setting the thermal efficiency to 0.75 for the solid model and 0.8 for the shell model, the experimental results were accurately reproduced for both models.

Table 3
Mechanical boundary condition.

Different directions	Fixed method
x-direction displacement	Fix at ①, ②, ③, ④
y-direction displacement	Bottom flange constrained Forced displacement on upper flange (−10 (mm))
z-direction displacement	Fix at ②, ④

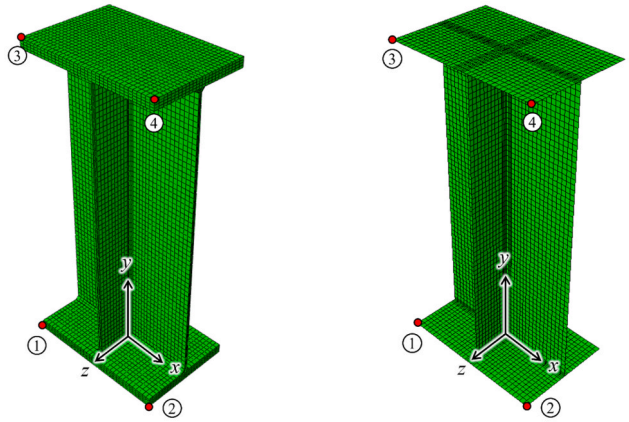

(a) Solid model (b) Shell model

Fig. 10. Elastic–plastic finite displacement analysis model.

4.2. Welding deformation

The out-of-plane welding deformation was measured at the edge of each vertical plate in six sections parallel to the weld line, as shown in Fig. 2 (b). Fig. 13 shows the out-of-plane welding deformations obtained from the experiments and analysis. In addition to the temperature history, the results for one specimen were simulated using an analysis. The magnitude of deformation was within 1.1 mm for plate thicknesses of 6 and 9 mm for each model, and a slight deformation due to welding was confirmed.

Furthermore, the amounts of deformation of the free edges of each web and stiffener were compared. Although the experimental results were reproduced in both solid and shell models, the maximum error percentage of the out-of-plane deformation of the solid model was 41.8%. Compared with the maximum error percentage of the shell model out-of-plane deformation of 12.7%, the shell model can better reproduce the out-of-plane deformation caused by welding.

4.3. Residual stress

Fig. 14 shows the welding residual stress obtained from the experiment and analysis. For each point representing the experimental data shown in Fig. 14, the average of four values from two specimens with the

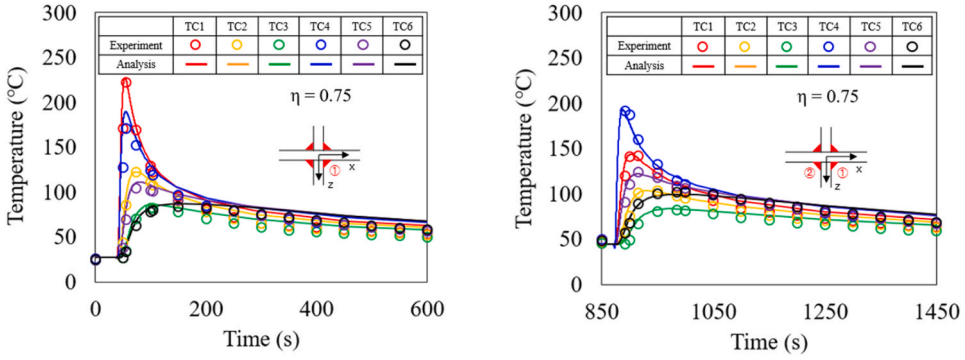

(a) First welding process (b) Second welding process

Fig. 11. Temperature histories at thermal couple locations predicted by FE model with solid element.

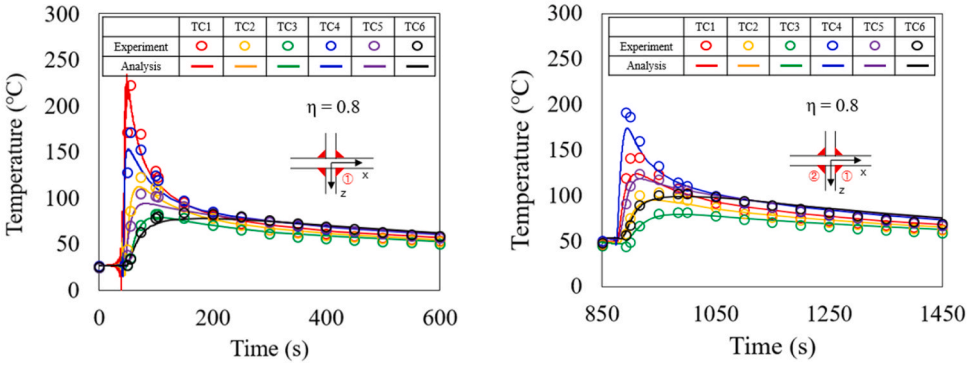

(a) The first welding process (b) The second welding process

Fig. 12. Temperature histories at thermal couple locations predicted by FE model with shell element.

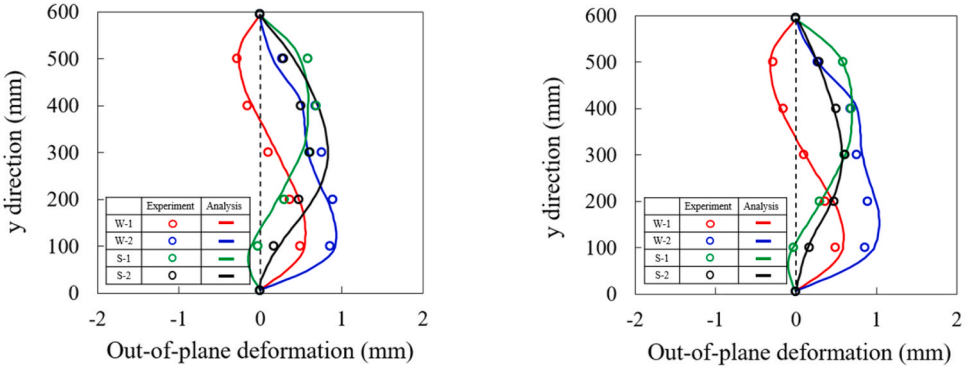

(a) Solid model (b) Shell model

Fig. 13. Welding out-of-plane deformation.

same locations in the web and stiffener panels was selected. For the web panel, approximately −59 MPa and −80 MPa of the residual stress was confirmed at $x = -150$ and 150 (mm). For the stiffener panel, approximately −74 MPa and −43 MPa of the residual stress was confirmed at $z = -80$ and 80 (mm). The compressive residual stresses measured in the experiment were reproduced using solid and shell models. The analytical tensile residual stresses around the welded parts between the web and stiffener were not compared with the experimental results because it was not feasible to measure them experimentally. The tensile stress of the solid model was larger than that of the shell model in the vicinity of the stiffener weld owing to the presence of the weld metal elements. The weld metal elements were considered in the solid model and provided a high tensile residual stress, whereas the weld metal was not formed in the shell model.

In this study, to discuss the influence of residual stress on the compressive behavior of cruciform columns, the analytical accuracy of

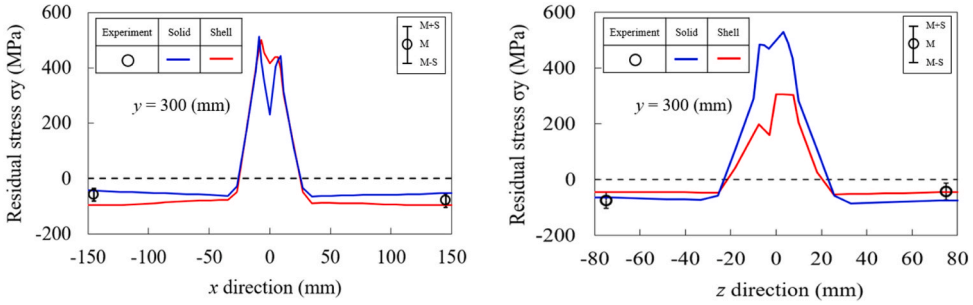

(a) Web (b) Stiffener

Fig. 14. Residual stress.

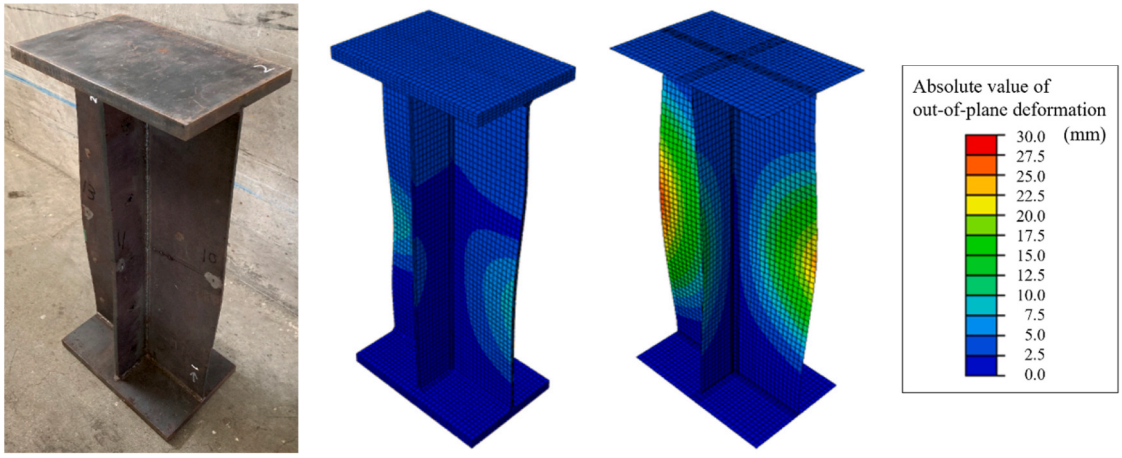

(a) Experimental specimen (b) Solid model (c) Shell model

Fig. 15. Deformation appearance after compression.

the compressive residual stress in the loading (y) direction (weld line direction) was investigated. In both the solid and shell models, the analytical results were in good agreement with the experimental results. Therefore, the compressive residual stress in the weld line direction could be approximately predicted.

4.4. Compressive behavior

The deformation modes obtained from the experiments and analyses are illustrated in Fig. 15. The figure depicts the final state after unloading for the experiment, while for the analysis, the state at maximum load is shown. In the shell model, the largely deformed parts are similar to those in the experimental results. However, in the solid model, the deformation of the vertical plate was smaller than that in the shell model, and the direction of the deformation was opposite to that in the experiment. This might be because the solid elements were not suitable for simulating the bending deformation owing to their larger shear stiffness compared to the shell elements [23].

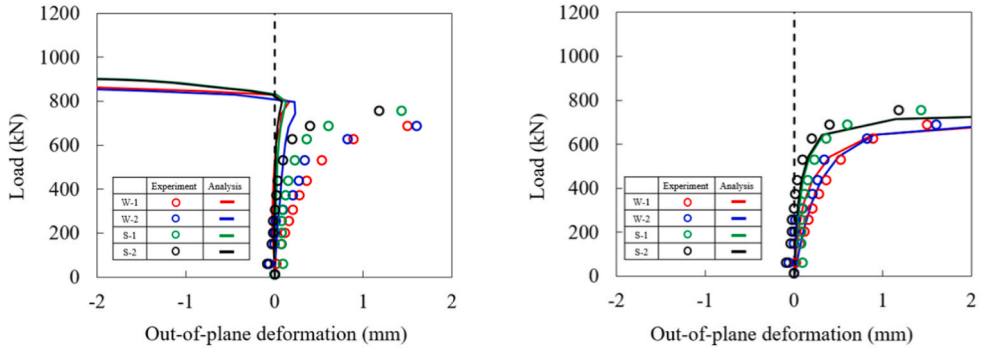

(a) Solid model (b) Shell model

Fig. 16. Out-of-plane deformation.

Fig. 16 shows the relationship between the load and out-of-plane deformation of the center of the free edge of the web and the stiffeners obtained by the experiment and analysis. The deformation in the clockwise direction along the *y*-axis was positive. The load-deformation curves of the shell model were close to the experimental results. Therefore, the out-of-plane deformation behavior can be accurately reproduced using the shell model.

The relationships between the load and vertical displacement obtained from the experiment and analysis are shown in Fig. 17. For each analysis model, the elastic stiffness values generally agreed with the experimental results. The maximum loads in the experiments were approximately 803 and 816 kN, respectively. The maximum loads in the solid and shell models were approximately 905 and 813 kN, respectively. The shell model showed a maximum load closer to the experimental results than the solid model.

Based on the deformation and load-displacement relationships, the solid model did not accurately replicate the deformation behavior and overestimated the maximum load. The deformation behavior observed in the experiment can be simulated using the shell model. The stiffness decreases sharply at a load of approximately 700 kN, as observed in the experiment. In addition, the maximum load of the shell model was approximately the same as the experimental value. Therefore, it can be concluded that the shell model effectively replicated the load-bearing behavior observed in the experimental specimen.

Using the same computer (3.50 GHz CPU, 6 cores), the simulation of the welding process and the compression behavior required a calculation time of 201,982 s (about 56 h) and 30,528 s (about 8.5 h) for the solid model and shell model, respectively. The calculation time of the shell model was approximately 15% of that required for the solid model. Therefore, utilizing the shell model can significantly reduce the analysis time.

4.5. Future works

The study highlights the potential of using shell elements for accurately predicting the compressive behavior of cross-sectional columns. However, further research is needed to verify the effect of simulating the welding process on the analysis accuracy. Future studies could focus on confirming the load-bearing behavior when considering only welding deformation as the initial condition, as well as when considering both welding deformation and residual stress. Additionally, continuous analysis of the welding process and compression behavior could be performed to improve analysis accuracy. The research could also be extended to bridge structural components using other welding methods, with the aim of reproducing actual bridge structures by combining different types of joints.

5. Conclusions

A series of experiments and analyses were conducted to investigate a highly accurate FE simulation method for steel structural members with welding imperfections. The main findings of this study are summarized as follows.

(1) A fillet-welding experiment was conducted using a cruciform steel column. The experiment was simulated by thermal elastic-plastic analysis using solid elements (solid model) and shell elements (shell model). The temperature history obtained from the experiment was reproduced using both analysis models. The out-of-plane welding deformation of the free edge was forcibly reproduced by adjusting the initial deformation. The welding residual stress at the center of the free side in the vertical direction obtained from the experiment was simulated using both the models.

(2) A monotonic static compressive loading experiment was performed on welded cruciform columns. After conducting the welding simulation using thermal elastic-plastic analysis, the compression experiment was simulated continuously. The reproducibility of the experiment was low when a solid model was used. In contrast, the shell model provided good agreement between the experimental and analytical results for the out-of-plane deformation and load–displacement relationships.

(3) The calculation time required for the continuous analysis of the welding process and compressive behavior of the shell model was 15% that of the solid model. It was confirmed that the shell model was highly effective in reducing the computation time required for the simulation.

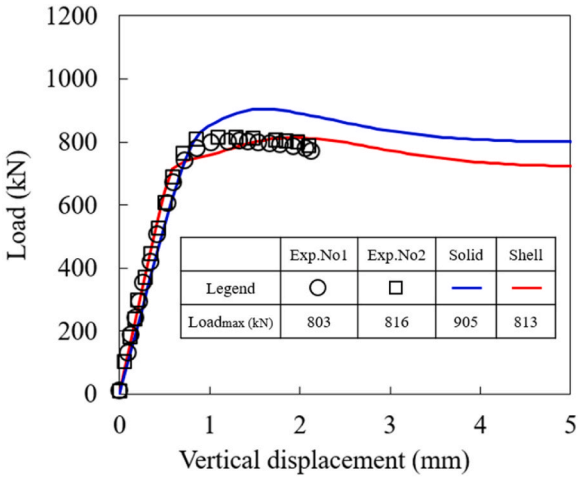

Fig. 17. Load and vertical displacement.

Author statement

As co-authors of this manuscript, we feel it is important to detail our specific contributions to the work. In this author statement, we will provide a clear and concise summary of the tasks we undertook, as follows. Experiment: S. Nozawa, Analysis: S. Nozawa and Y. Cheng; Methodology: Y. Cheng, S. Nozawa, and M. Hirohata; Validation: Y. Cheng, S. Nozawa, and M. Hirohata; Original draft preparation: S. Nozawa and Y. Cheng; Review and editing: Y. Cheng and M. Hirohata; Visualization: Y. Cheng; Supervision: M. Hirohata; Project administration: M. Hirohata.

Declaration of competing interest

The authors declare that they have no known competing financial interests or personal relationships that could have appeared to influence the work reported in this paper.

Data availability

The data that has been used is confidential.

References

[1] T. Yao, P.I. Nikolov, Y. Miyagawa, Mechanical Effects of Welding, Springer, Heidelberg, 1992, pp. 261–268.
[2] Y. Ueda, W. Yasukawa, T. Yao, H. Ikegami, R. Ohminami, Effects of welding residual stresses and initial deflection on rigidity and strength of square plates subjected to compression (Report II), Trans. JWRI 6 (1) (1977) 33–38.
[3] Y. Ueda, T. Yao, The influence of complex initial deflection modes on the behaviour and ultimate strength of rectangular plates in compression, J. Constr. Steel Res. 5 (4) (1985) 265–302.
[4] J.K. Paik, A.K. Thayamballi, Ultimate Limit State Design of Steel-Plated Structures, John Wiley & Sons, San Ramon, 2003.

[5] P. Ferro, F. Bonollo, A. Tiziani, Methodologies and experimental validations of welding process numerical simulation, Int. J. Comput. Mater. Sci. Surf. Eng. 3 (2–3) (2010) 114–132.
[6] C.Y. Wei, W.G. Jiang, Influence of welding groove on residual stress and distortion in T-joint weld, in: IOP Conference Series: Materials Science and Engineering vol. 733, IOP Publishing, Shanghai, 2020, 012010.
[7] A.J. Sadowski, J.M. Rotter, Solid or shell finite elements to model thick cylindrical tubes and shells under global bending, Int. J. Mech. Sci. 74 (2013) 143–153.
[8] M. Hirohata, Y. Itoh, High effective FE simulation methods for deformation and residual stress by butt welding of thin steel plates, Engineering 6 (9) (2014) 507–515.
[9] M. Hirohata, Y. Itoh, A simplified FE simulation method with shell element for welding deformation and residual stress generated by multi-pass butt welding, International Journal of Steel Structures 16 (1) (2016) 51–58.
[10] M. Hirohata, S. Nozawa, Y. Tokumaru, Verification of FEM simulation by using shell elements for fillet welding process, Int. J. Interact. Des. Manuf. 16 (2022) 1–13.
[11] Japan Road Association, Specifications for Highway Bridges Part II Steel Bridges, Maruzen Publishing, Tokyo, 2012 (In Japanese).
[12] R. Bai, Z. Guo, C. Tian, et al., Investigation on welding sequence of I-beam by hybrid inversion, Mar. Struct. 62 (2018) 23–39.
[13] B. Chen, C.G. Soares, Effect of welding sequence on temperature distribution, distortions, and residual stress on stiffened plates, Int. J. Adv. Manuf. Technol. 86 (2016) 3145–3156.
[14] G. Fu, M.I. Lourenço, Influence of the welding sequence on residual stress and distortion of fillet welded structures, Mar. Struct. 46 (2016) 30–55.
[15] H. Nakagawa, H. Suzuki, Ultimate temperatures of steel beams subjected to fire, Steel Construction Engineering 6 (22) (1999) 57–65.
[16] Y.C. Kim, J.Y. Lee, K. Inose, The high accurate prediction of welding distortion generated by fillet welding, Q. J. Jpn. Weld Soc. 23 (3) (2005) 431–435.
[17] M.P. Aung, H. Katsuda, M. Hirohata, Fatigue-performance improvement of patch-plate welding via PWHT with induction heating, J. Constr. Steel Res. 160 (2019) 280–288.
[18] M. Hirohata, F. Takeda, M. Suzaki, K. Inose, N. Matsumoto, D. Abe, Influence of laser-arc hybrid welding conditions on cold cracking generation, Weld. World 63 (2019) 1407–1416.
[19] M. Hirohata, Effect of post weld heat treatment on steel plate deck with trough rib by portable heat source, Weld. World 61 (6) (2017) 1225–1235.
[20] M.M. Pastor, J. Bonada, F. Roure, M. Casafont, Residual stresses and initial imperfections in non-linear analysis, Eng. Struct. 46 (2013) 493–507.
[21] H. Akima, A new method of interpolation and smooth curve fitting based on local procedures, J. ACM 17 (4) (1970) 589–602.
[22] Japan Welding Society, Welding and Joining Handbook, second ed., Maruzen Publishing, Tokyo, 2003 (In Japanese).
[23] W. Jiang, G. Bao, J.C. Robert, Finite element modeling of stiffened and unstiffened orthotropic plates, Comput. Struct. 63 (1) (1997) 105–117.